Advances in Geo-Energy Research

Vol. 15, No. 3, p. 273-282, 2025

Original article

Dissolution patterns prediction for horizontal rough fracture based on deep neural network and lattice Boltzmann method

Gaowei Yi[1], Xinlin Zhuang[2], Da Zhang[1,3], Yan Li[1]*, Liang Gong[4]*

[1]*College of Engineering, Ocean University of China, Qingdao 266000, P. R. China*

[2]*School of Computer Science and Technology, East China Normal University, Shanghai 200062, P. R. China*

[3]*Department of Mechanical Engineering, National University of Singapore, Singapore 119260, Singapore*

[4]*College of New Energy, China University of Petroleum (East China), Qingdao 266580, P. R. China*

Keywords:
Lattice Boltzmann method
fully connected neural network
gas-liquid phase change
dissolution reaction

Cited as:
Yi, G., Zhuang, X., Zhang, D., Li, Y., Gong, L. Dissolution patterns prediction for horizontal rough fracture based on deep neural network and lattice Boltzmann method. Advances in Geo-Energy Research, 2025, 15(3): 273-282.
https://doi.org/10.46690/ager.2025.03.09

Abstract:
Understanding thermal energy transfer and fracture evolution in submarine hydrothermal systems is essential for sustainable resource utilization, but simulating these complex multiphase, multi-physics processes is challenging. This study integrates the lattice Boltzmann method with a fully connected neural network to investigate hydrothermal phase separation and its effects on chemical dissolution in carbonate fractures at the pore scale. Specifically, the lattice Boltzmann method simulates gas-liquid phase separation induced by seawater boiling, affecting carbonate fracture dissolution at the pore scale. The fully connected neural network predicts the resulting fracture geometry and dissolution quantities under various physical conditions. Analysis of simulation datasets demonstrates that the fully connected neural network achieves high predictive accuracy, with a total loss of 0.01 and reduces computation time by over 20% compared to traditional methods. The coupled lattice Boltzmann method-fully connected neural network model effectively simulates fractures with sizes ranging from millimeters to centimeters, excelling in handling chemical dissolution, multiphase flows, and multicomponent interactions. This approach offers valuable predictive capabilities for applications such as enhanced geothermal systems and oil reservoir exploitation.

1. Introduction

Submarine hydrothermal systems play a crucial role in renewable energy exploration and marine resource development, serving as significant sources of thermal energy (Lowell et al., 1995). These systems are essential for global heat transfer, mineral formation, and marine ecosystem dynamics (Spitzmüller et al., 2021). A comprehensive understanding of the complex interactions among fluid flow, heat transfer, and rock dissolution in these systems is critical for various applications, including thermal energy extraction from submarine hydrothermal vents, reservoirs management, and mineral resources assessment. Within submarine hydrothermal systems, seawater undergoes substantial physical and chemical changes as it circulates through underground fractures and rock strata. Under high temperature and pressure conditions, phase separation occurs (Zhang et al., 2019), generating complex multiphase flow patterns within fractures. This phase separation process significantly affects water-rock interactions (Mahmoodi et al., 2018), particularly carbonate minerals dissolution, thereby modifying fracture geometry and permeability. However, accurately modeling the coupled effects of phase separation, chemical reactions, and fracture evolution remains a major challenge for traditional methods.

Direct observation of hydrothermal circulation in deep-sea

Yandy Scientific Press

*Corresponding author.
E-mail address: yigaowei@stu.ouc.edu.cn (G. Yi); xinlinzhuang@stu.ecnu.edu.cn (X. Zhuang); zhangdazd@sohu.com (D. Zhang); yanli@ouc.edu.cn (Y. Li); lgong@upc.edu.cn (L. Gong).

Received December 23, 2024; revised January 28, 2025; accepted February 25, 2025; available online March 3, 2025.

environments remains inherently difficult, making numerical simulation essential for understanding of these processes. Previous simulation studies have explored hydrothermal circulation, plume dynamics, and mineral precipitation, shedding light on key characteristics of hydrothermal systems (Zeng et al., 2023; Luo et al., 2024). However, computational constraints and the complexity of the underlying physical phenomena (Liu and Liu, 2016), particularly the comprehensive modeling of coupled multi-physics processes at the mesoscale, pose significant challenges. Moreover, to effectively apply numerical simulations in geothermal development and reservoir management, it is necessary to develop computational frameworks capable of efficiently and accurately predicting dissolution patterns under various conditions (Gong et al., 2023). Traditional computational fluid dynamics methods struggle to resolve complex interfacial phenomena and chemical reactions at the pore scale (Xi et al., 2021; Micale et al., 2022). The lattice Boltzmann method (LBM) has emerged as a powerful approach for simulating multiphase flows and reactive processes at the mesoscale, clarifying underlying mechanisms and evolution (Zhang et al., 2021a). LBM is particularly well-suited for handling complex geometries and boundaries, as well as capturing multiphase flows and phase separation (Fu et al., 2024). It is also adept at dealing with multiple coupled physical processes fluid flow (Bhadauria et al., 2021), heat transfer (Sharma et al., 2020), and chemical reactions (Chen et al., 2013)). Despite these advantages, LBM's computational cost remains a significant drawback, particularly for large-scale or long-term simulations (Mohammadi-Arani et al., 2024). Furthermore, it is prone to disturbances that can lead to divergence in simulation results, restricting its usen in some scenarios.

Recent advances in artificial intelligence, particularly in deep learning, have facilitated the integration of machine learning techniques with numerical simulation methods, offering a promising avenue for enhancing the modeling and prediction of complex geophysical processes (He et al., 2019). Machine learning has been successfully applied in subsurface engineering, including well log analysis (Xie et al., 2024), reservoir characterization (Wang et al., 2023), and production optimization (Wang and Chen, 2023), demonstrating strong adaptability to complex multi-physics and multiphase challenges (Elrahmani et al., 2024). Among these ML methods, fully connected neural networks (FCNNs) excel due to their robust representational capacity (Hinton et al., 2006; Salakhutdinov and Hinton, 2009). FCNNs effectively model complex nonlinear relationships between multiple physical quantities (such as density, velocity, temperature, etc.) generated by LBM and the predicted dissolution states by learning from large datasets. Unlike Convolutional Neural Networks, FCNNs are better suited for non-spatially structured parameter relationships, and they outperform Recurrent Neural Networks in computational efficiency for steady-state or quasi-steady-state problems (Yi et al., 2024). Additionally, FCNNs enable real-time data processing and exhibit strong predictive capabilities, allowing them to quickly adapt to new and changing conditions without extensive recalibration. This allows them to demonstrate superior adaptability and efficiency in handling complex engineering application (Kamrava et al., 2021; El-Amin et al., 2023; Elrahmani et al., 2024).

This study proposes an innovative integration of FCNNs with LBM to simulate thermo-hydro-chemical multiphase reactions in submarine hydrothermal systems, enabling the accurate prediction of fracture dissolution patterns. The optimized model architecture balances the physical accuracy of LBM with the computational efficiency of FCNN. This study's key contributions are threefold: First, it pioneers the coupling of deep neural networks with LBM to predict dissolution processes in submarine hydrothermal systems. Second, it employs an FCNN to capture the complex variations during the dissolution process, with a detailed analysis of the FCNN architecture and hyperparameter optimization. Third, it systematically evaluates the dissolution process under various parameter settings, rigorously assessing the model's robustness and demonstrating its applicability and reliability in real-world scenarios. This approach provides valuable simulation insights and practical tools for engineers working in geothermal resource development and reservoir management.

2. Modeling dissolution process

Submarine hydrothermal systems represent a pivotal subject of inquiry within the vanguard of Earth sciences, offering insights into the intricate interactions between deep-seated geological processes and marine environments (Martín-Díaz et al., 2024). These systems serve as reservoirs of substantial thermal and mineral resources and are governed by hydrothermal processes such as gas-liquid phase separation, mineral precipitation, and dissolution Numerical studies have investigated phase separation on water-rock interactions in pores and rough fractures, analyzing the influence of various factors on the heat and mass transfer reactions of multiphase hydrothermal flows (Liu et al., 2024). To further investigate these phenomena, this study employs the LBM, a microscopic particle-based approach in computational fluid dynamics, which effectively simulates multiphase flows and interfacial phenomena. This section first presents the derivation of using the LBM for computing dissolution processes, and then introduces the task formulation in FCNN.

2.1 LBM numerical method

In this study, seawater is modeled as an acidic brine solution. Given its relatively low concentration, it is assumed that ionic mass transfer has a negligible effect on fluid behavior. To simulate seawater flow with exhibiting phase-change characteristics, a distribution function model is employed: The LBM relies on its core evolution equation, which underpins the simulation and prediction of fluid dynamics. The evolution equation for the density distribution function within a multiphase multicomponent LB model is outlined as (Shan and Chen, 1993):

$$f_i^{\sigma}(x+e_i\delta_t,t+\delta_t)-f_i^{\sigma}(x,t)= -\frac{1}{\tau^{\sigma}}\left[f_i^{\sigma}(x,t)-f_i^{eq,\sigma}(x,t)\right]+\Delta f_i(x,t) \quad (1)$$

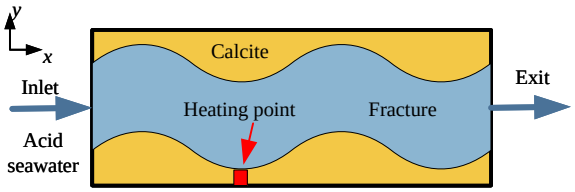

Fig. 1. Fracture geometry model diagram.

where $f_i^{\sigma}(x,t)$ is the density distribution function of fluid component σ at position x and time t; δ_t is the lattice step time step length; e_i is the discrete velocities; τ is the relaxation time. $f_i^{eq,\sigma}$ represents the density distribution function in equilibrium:

$$f_i^{eq,\ \sigma}(x,t) = \omega_i \rho_\sigma \left[1 + \frac{e_i \cdot u_\sigma}{c_s^2} + \frac{(e_i \cdot u_\sigma)^2}{2c_s^4} - \frac{u_\sigma^2}{2c_s^2}\right] \quad (2)$$

where ω_i is the weighting factor; ρ_σ and u_σ respectively denote the macroscopic density and velocity of fluid component σ; $c_s = 1/\sqrt{3}$ is the lattice speed. In the LBM framework, fluid flow is modelled using the density distribution function alongside the continuity equation:

$$\rho_\sigma = \sum f_i^{\sigma} \quad (3)$$

$$\rho_\sigma u_\sigma = \sum_i e_i f_i^{\sigma} + \frac{\delta_t}{2} F^{\sigma} \quad (4)$$

where F^{σ} is the total external force exerted on the fluid component σ (Zhang et al., 2021b).

To address thermal effects during phase separation, the LBM energy equation models the temporal evolution of the temperature field, incorporating thermal conduction and heat source terms (Zhou et al., 2020b):

$$\frac{\partial T}{\partial t} + \nabla \cdot (u_\sigma T) = \nabla \cdot (\alpha \nabla T) + \phi_1 + \phi_2 \quad (5)$$

where T is the temperature; ϕ_1 and ϕ_2 respectively represent the source terms for gas-liquid phase transition and reaction heat; α denotes the thermal diffusivity coefficient. The variations and spatial distribution of solute ion concentrations over time within hydrothermal fluids are characterized, within the mass transfer LBM model:

$$\frac{\partial C}{\partial t} + (u_\sigma \cdot \nabla) C = D \Delta C \quad (6)$$

where C signifies the ion concentration; D represents the solute diffusion coefficient. In hydrothermal reaction zones, these fluids typically exhibit acidic properties, enriched with hydrogen ions that drive dissolution reactions with rocks, such as calcite. The simulation of dissolution reactions is expressed through the following equation:

$$H^+ + CaCO_3 = Ca^{2+} + HCO_3^- \quad (7)$$

The chemical reaction process is characterized as a first-order kinetic reaction at the acid-fluid-solid interface. The reaction occurs exclusively at the liquid-solid boundary, and the boundary conditions can be described by the following equation (Zhou et al., 2020a):

$$D \frac{\partial C}{\partial n} = -k_r (C - C_{eq}) \quad (8)$$

where C_{eq} is the ion concentration at equilibrium. The rate of reaction for dissolution at the scale of pores is largely dictated by the discrepancy in concentration from the current state to that at equilibrium. And under conditions that are not isothermal, the constant rate of reaction k_r, is characterized through the Arrhenius equation (Kang et al., 2010).

The solid mass change induced by dissolution reactions are quantified using a volumetric approach, which can be implemented through the volume-of-pixel method (Zhang et al., 2021b), as expressed below. If the solid phase mass falls below zero, it is considered fully dissolved:

$$\frac{\partial y}{\partial t} = -MSk_r (C - C_{eq}) \quad (9)$$

where y is the mass of calcite per unit lattice; M represents the molar mass of calcite and S is the reaction area.

2.2 Fracture geometry model

This study develops a detailed fracture geometry to simulate hydrothermal reactions and phase separation in submarine hydrothermal systems, as shown in Fig. 1. The model consists of interconnected fracture channels representing the fractures and pores within suboceanic bedrock (Coronado et al., 2011), designed as two-dimensional planar structures. The fracture dimensions are determined based on geological data from actual submarine hydrothermal vent regions, with selected representative fracture sizes of 1.2 cm in width and 3 cm in length, to balance computational efficiency and model complexity. This study posits the roughness of the fractures as regular rather than random (following a sinusoidal distribution) to mitigate the effects of fracture roughness. A heat source is positioned along lower boundary of the fracture to simulate the conditions of a heated wall and phase separation zones. The fractures are assumed to be fully interconnected, allowing for fluid ingress and egress through the defined inlet and outlet boundary conditions.

In this model, a uniform velocity boundary condition is imposed at the inlet, while a fully developed boundary condition is applied at the outlet. Fluid-solid interactions at the midstream interface are modeled using bounce-back boundary conditions. Initially, the system consists of a saturated, static liquid at ambient temperature, with no chemical reactions. The solid boundaries maintain a constant temperature. At the inlet, a non-equilibrium bounce-back scheme is employed to preserve ambient temperature, while convective boundary conditions regulate fluid outflow at the outlet. The temperature field is initialized as a developed profile, and a constant acid concentration boundary is imposed at the inlet.

This fracture geometry model accurately captures phase separation processes within the fracture, including hydrothermal phase separation, water-rock dissolution, and solute migration. In the construction of the LBM-FCNN method, it is necessary to first utilize these LBM equations for simulations, thereby generating a comprehensive dataset of simulation results. Subsequently, this dataset is employed to train FCNN models for the prediction of fluid dynamics, phase separation, solute transport, fracture wall changes, reaction dynamics, and solid mass variations.

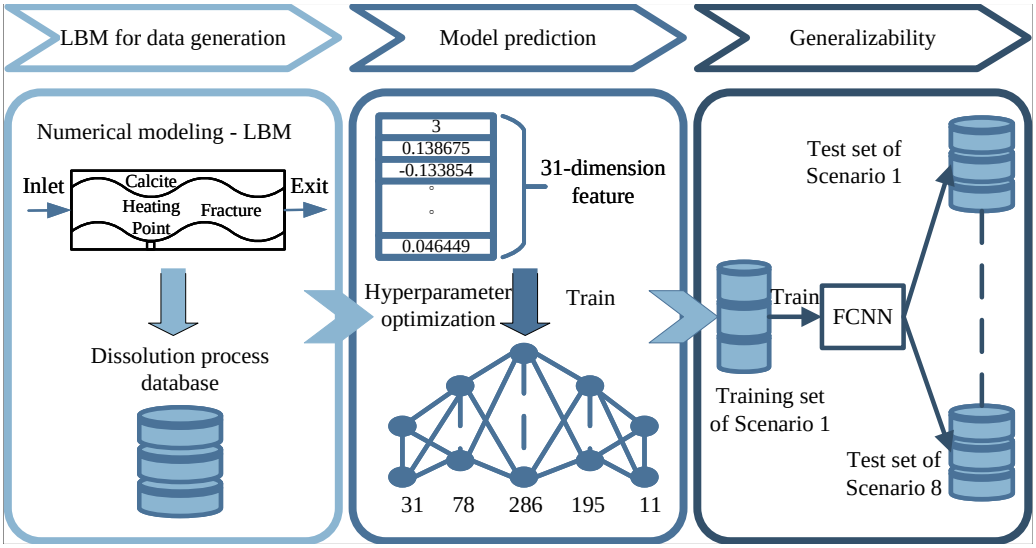

Fig. 2. Workflow overview: LBM simulations for dissolution dataset generation, FCNN model training, and generalizability analysis.

2.3 Simulation by the LBM

This study investigates the effects of hydrothermal fluid dynamics and phase separation on fracture dissolution, focusing on the interplay between multiphase flow and chemical kinetics. Acidic ions (H^+) in seawater react with carbonate minerals ($CaCO_3$), dissolving them into the fluid phase and altering fracture structure and composition. The validity of the numerical model used in this study has been confirmed (Zhang et al., 2021b). Simulations reveal that nucleate boiling at the heat source produces bubbles that rise from the fracture base to the crest, where foam accumulation hinders acidic interactions. However, phase separation increases liquid acidity by releasing acid-base ions during gas evolution, enhancing dissolution. Additionally, the exothermic nature of phase separation accelerates chemical reactions, moderately promoting mineral dissolution.

The LBM has been employed for detailed mesoscopic simulations of fluid dynamics and phase transitions within fractures, where even relatively small fractures require tens of thousands of grid points to accurately resolve fluid physics and chemical reactions. This granularity incurs high computational costs for prolonged simulations and limits adaptability to rapid changes. In contrast, the FCNN model leverages the data-driven nature of machine learning to extract complex patterns from data, significantly lowering computational demands and enhancing scalability across diverse conditions. This study predicts total dissolution to assess mass transfer and its effects on regional permeability. It also examines dissolution patterns on fracture walls, uncovering microscale changes in processes like fluid percolation. Factors including inlet velocity, wettability, and fracture aperture are analyzed to understand their influence on dissolution, enabling predictions of mass transfer and fracture evolution. Based on these insights, eight scenarios have been designed for comprehensive analysis.

3. Deep learning as problem solver

The complete workflow of our proposed method is depicted in Fig. 2. Initially, the LBM is employed to construct the dataset. The dataset is divided into three subsets: Training, validation, and test. The training set trains the models, the validation set optimizes hyperparameters and test set evaluates performance. A comprehensive analysis in the final stage assesses the generalizability and robustness of the optimized FCNN model.

3.1 Machine learning task definition

In the domain of FCNN, our task is formulated as a regression task where the objective is to predict continuous output Y based on given input X. Both input and output are multi-dimensional arrays derived from measured values representing material properties of the under study.

The input is designed as 31-dimensional features, including a timestep and six distinct five-dimensional arrays, each representing specific attributes of the dissolution process.

1) An array representing the upper bound metrics.
2) An array capturing the lower bound metrics.
3) An upper threshold array measured for validation.
4) A lower threshold validation array.
5) Array of physical variables.
6) An array consisting of edge detection results.

This study investigates a comprehensive set of parameters that critically influence the simulation and prediction of hydrothermal dissolution. These parameters range from fundamental physical properties, such as fluid velocity and viscosity, to complex dynamics, including phase transitions and chemical reactions. This diverse parameter set highlights the complexity of the underlying physical phenomena and showcases the FCNN's ability to model and adapt to varied scenarios effectively. By training diverse LBM datasets, the FCNN rapidly adjusts to operational parameter changes. This

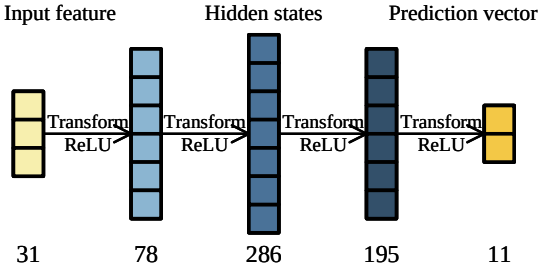

Fig. 3. The architecture of our optimal FCNN model obtained through hyperparameter optimization (ReLU is applied as activation functions for each layer.).

Table 1. Eight different scene hyperparameter values.

Scenarios	Inter velocity (10^{-4} m/s)	Contact angle (°)	Fracture width (10^{-2} m)
1	2.0	18.0	1.2
2	3.0	18.0	1.2
3	4.0	18.0	1.2
4	3.0	25.2	1.2
5	3.0	32.4	1.2
6	3.0	18.0	0.8
7	3.0	18.0	1.0
8	3.0	18.0	1.4

adaptability not only enhances the model's applicability in dynamic environments but also significantly reduces the time and computational cost associated with recalibration.

The target output Y comprises of two continuous variables, forming an 11-dimensional vector that includes the upper and lower fracture wall positions and dissolved volume. Each input parameter directly influences fluid dynamics, mass transfer, or the chemical reactions, with interdependencies among them. All parameters are quantifiable and measured in real systems, ensuring that model balances computational efficiency and engineering applicability.

1) An array denoting the volume solids above the set limits, encapsulated within a five-unit array.
2) An array representing the volume solids below the set thresholds, also segmented into a five-unit array.
3) A scalar representing the average dissolution percentage.

3.2 Method

This section outlines the core design of the proposed FCNN (Yamashita et al., 2018), focusing on its ability to reveal intricate relationships among diverse features. At the heart of deep learning models lies the FCNN, a cornerstone architecture known for its simplicity and effectiveness. It consists of layers where each neuron connects to every neuron in the adjacent layer, earning the designations "fully-connected" or "dense" due to this extensive interconnectivity. This full connectivity indicates that each neuron receives outputs from all neurons in the antecedent layer, executes a weighted summation of these inputs, and then processes the result via a nonlinear activation function to produce an output. The FCNN comprises three primary components: The input layer, the hidden layer, and the output layer. The input layer receives raw data or features. The hidden layer serves to extract advanced features. The output layer delivers the final prediction results. In this study, the input layer processes the dissolved feature vector, the hidden layer analyzes it, and the output layer yields the predicted system values. The dense computation process in each layer is denoted as:

$$Z^{[l]} = W^{[l]} h^{[l-1]} + b^{[l]} \tag{10}$$

$$a^{[l]} = g^{[l]}(Z^{[l]}) \tag{11}$$

where $Z^{[l]}$ represents the weighted sum in layer l; $W^{[l]}$ is the weight matrix linking layer l-1 and layer l; $h^{[l-1]}$ denotes the output vector from the preceding layer l-1; $b^{[l]}$ is the bias vector of layer l; $a^{[l]}$ is the ultimate output vector of layer l and $g^{[l]}$ signifies the activation function within layer l.

By increasing the number of hidden layers and augmenting the number of neurons, FCNNs enhance their ability to capture complex, nonlinear relationships. This expanded architecture the network to learn deeper, more abstract feature representations, enhancing predictive performance. However, general design principles may not fully suit the specific requirements of this task. To further strengthen this capability, systematic experimentation was conducted, including extensive hyperparameter optimization. Specifically, the dimensionality of the hidden layers within the FCNN architecture was optimized to achieve more robust and reliable results. The structure of the optimized FCNN, obtained through this hyperparameter tuning process, is illustrated in Fig. 3.

4. Experiment

To foster collaborative and support the inclusivity of the open-source community. The source code associated with this paper has been made publicly accessible at https://github.com/mihara-bot/DISS.

4.1 Experimental dataset

The dataset used in this study is derived from LBM simulations, covering eight distinct real-world scenarios detailed in Table 1. Three parameters, varied across these scenarios, represent critical factors affecting dissolution and fluid flow within the fracture at the physical level. By treating these as hyperparameters, the machine learning model captures the coupled effects of flow conditions, fluid properties, and geometrical constraints on dissolution patterns and dynamics. Each scenario yields a curated subset of 4,500 timesteps, producing a total dataset of 36,000 samples. This dataset was split into training, and test sets at an 8 : 1 : 1 ratio. The training set supports model learning, the validation set guides hyperparameter optimization, and the test set provides an independent measure of final model performance.

4.2 Evaluation metrics

In this study, model performance was evaluated for prediction accuracy using three standard regression metrics: mean

Table 2. Fixed hyperparameters used during training.

Hyperparameter	Value
Size of training set	28,800
Size of development set	3,600
Size of test set	3,600
Batch size	32
Learning rate	1e-4
Training epoch	{50, 80, 100}
Optimizer	Adam

Table 3. Hyperparameter optimization configuration details of FCNN.

Hyperparameter	Value type	Value range
Number of hidden layers	Integer	{1, 2, 3, 4}
Number of neurons in each hidden layer	Integer	[32, 512]
Dropout rate	Float	[0, 0.5]

Table 4. Optimal hyperparameters details of FCNN.

Hyperparameter	Value type	Exact value
Number of hidden layers	Integer	3
Number of neurons in layer 1	Integer	78
Number of neurons in layer 2	Integer	286
Number of neurons in layer 3	Integer	195
Dropout rate in layer 1	Float	0.0062
Dropout rate in layer 2	Float	0.0074
Dropout rate in layer 3	Float	0.0038
Training epoch	Integer	100

squared error (MSE), mean absolute error (MAE), and mean absolute percentage error (MAPE). These metrics measure the difference between predicted and corresponding reference values (the gold standard obtained via LBM), calculated independently on test dataset by averaging normalized deviations. Notably, MAPE is expressed as a percentage to reflect relative error. These three metrics can be calculated as:

$$\mathrm{MSE}(\dot{y},\hat{y}) = \frac{1}{n}\sum_{i=1}^{n}(\dot{y}-\hat{y})^2 \tag{12}$$

$$\mathrm{MAE}(\dot{y},\hat{y}) = \frac{1}{n}\sum_{i=1}^{n}|\dot{y}-\hat{y}| \tag{13}$$

$$\mathrm{MAPE}(\dot{y},\hat{y}) = \frac{1}{n}\sum_{i=1}^{n}\left|\frac{\dot{y}-\hat{y}}{\dot{y}}\right|\cdot 100 \tag{14}$$

where n represent the total number of samples in the test dataset; $\dot{y}$ is the actual value and $\hat{y}$ is the predicted value.

4.3 Training configuration

The model training configuration encompasses both hardware and software specifications. The hardware includes an Ubuntu 22.04 LTS server with an Intel(R) Xeon(R) CPU E5-2620 v3@2.40GHz, 32GB of RAM, and an NVIDIA GeForce RTX 2080Ti GPU. The software configuration employs PyTorch 1.13.0 for model implementation, ensuring compatibility with other supported versions, alongside training scripts developed in Python 3.9.18. Additionally, the fixed hyperparameters used during the training phase are summarized in Table 2.

4.4 Hyperparameter optimization configuration

Hyperparameter optimization during training utilized the Optuna framework (Akiba et al., 2019) to maximize model performance. Optuna implements Sequential Model-based Optimization, combining sequential modeling with model-based techniques. This method iteratively samples parameter values from the search space, assesses their performance, and refines prediction of parameter-outcome relationship, enabling efficient exploration of the hyperparameter space. Its scalability and adaptability support optimization across diverse parameter types, making it an effective tool for hyperparameter tuning.

The optimized hyperparameters include the number of hidden layers in the model, the number of neurons in each hidden layer, and the dropout rate, which is a technique to prevent the model from memorizing the data too closely (known as overfitting), applied after each layer. Given the dataset size and task requirements, a simpler, shallower FCNN design was selected. Further details can be found in Table 3.

4.5 Main results

As described in Sections 4.1 and 4.2, hyperparameter optimization was performed 50, 80, and 100 epochs, with 500 trials per search to determine optimal hyperparameters for the given scenario. Results in Table 4 indicate that these optimal hyperparameters are somewhat unexpected, highlighting the advantage of optimization over manual design model training.

The training process of the optimal FCNN is illustrated in Fig. 4, while Table 5 reports performance metrics for the three optimal models across different training epochs. Fig. 5 further illustrates the training results of the best FCNN, comparing the positional variations of the upper and lower walls of the simulated fracture predicted by the machine learning model against the results obtained from the LBM. The training trajectory demonstrates remarkable stability, with minimal fluctuations, indicating consistent model convergence. This optimal model excels in all three evaluated metrics having the fewest parameters, underscoring its efficiency and effectiveness. Additionally, in terms of real-time computational cost, the FCNN is at least 20% more efficient than the LBM. Unlike the LBM, which requires meticulous parameter tuning and grid setup for each new scenario. The FCNN model gen eralizes effectively from simulation datasets to new conditions, cutting computation time and cost. To apply it in real-world tasks, also need to conduct additional training using data collected from reality.

All results in this table reflect model training with optimal

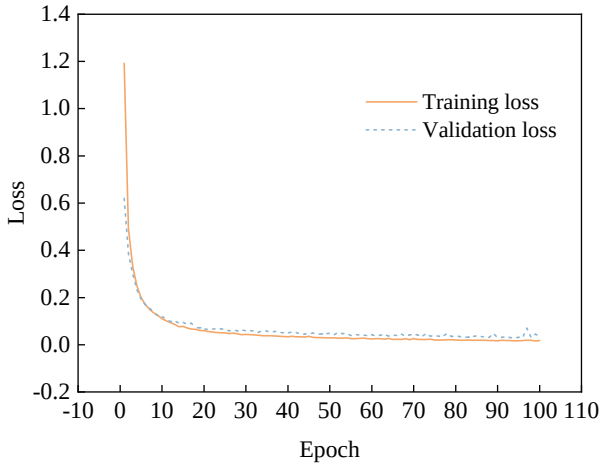

Fig. 4. The process of training optimal model.

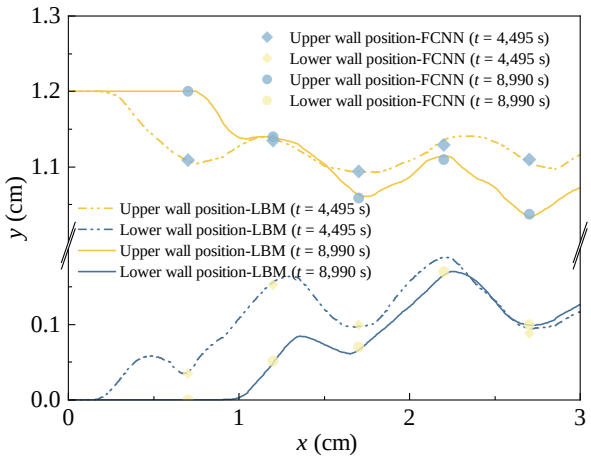

Fig. 5. LBM simulated up and down position change comparison with FCNN predicted points.

Table 5. Results of optimal FCNN under different training epochs.

Training epoch	Number of parameters	MSE	MAE	MAPE
50	141,587	0.0371	0.0660	0.0972
80	149,877	0.0289	0.0579	0.0826
100	83,211	0.0226	0.0476	0.0578

hyperparameters, averaging over 10 runs to reduce errors from randomness.

5. Analysis

5.1 Effects of longer training

Typically, a deep learning model progressively fits the target distribution, its performance tends to improve with more training epochs-up to the point before overfitting occurs. The investigation into the potential for enhanced model performance through extended training involved increasing the number of training epochs from 100 to a maximum of 500, with increments of 50 epochs, as detailed in Table 6. A clear trend of performance improvement is observed with increasing epochs, particularly in accuracy metrics, up to a threshold. Optimal performance is achieved at 450 epochs, with the lowest MSE (0.0119), MAE (0.0219), and MAPE (0.0299), reflecting peak prediction accuracy. The second-best performances occur at 350 epochs for MSE (0.0128) and at 400 epochs for both MAE (0.0259) and MAPE (0.0332). Beyond 450 epochs, performance slightly declines, indicating diminishing returns and possible overfitting.

While training for additional multiple epochs can yield performance improvements, it requires significantly more computational resources. This trade-off underscores a fundamental consideration in machine learning: Beyond a certain threshold, the marginal gains in performance may not offset the increased computational cost and time. In this study, the slight improvements in MSE, MAE, and MAPE metrics beyond the optimal 450 epochs incur higher resource costs. These findings highlight the importance of hyperparameter optimization strategies that balance performance gains with computational efficiency, supporting cost-effective real-world applications.

Table 6. Results of FCNNs under each optimal hyperparameter optimization scenario.

Training epoch	MSE	MAE	MAPE
100	0.0226	0.0476	0.0578
150	0.0138	0.0419	0.0526
200	0.0148	0.0307	0.0407
250	0.0172	0.0376	0.0445
300	0.0171	0.0353	0.0438
350	0.0128	0.0329	0.0426
400	0.0170	0.0259	0.0332
450	0.0119	0.0219	0.0299
500	0.0132	0.0291	0.0368

Results are highlighted with the best outcomes in bold and second-best outcomes underlined for clarity.

5.2 Generalization of FCNN

The study extended its focus to a detailed analysis of models trained on individual scenario-specific datasets, following the established superior predictive performance of the optimal model when trained on the comprehensive dataset encompassing all eight scenarios. This investigation examines two main aspects: The predictive accuracy of a model when trained and tested within the same scenario, and the generalization ability of a model trained in one scenario (e.g., Scenario A) when applied to a different scenario (e.g., Scenario B).

5.2.1 Performance within same scenario

This study trained eight models on datasets from eight scenarios, adhering to the settings in Section 4.1 and Table 1, with training process depicted in Figs. 6(a)-6(d). Model per-

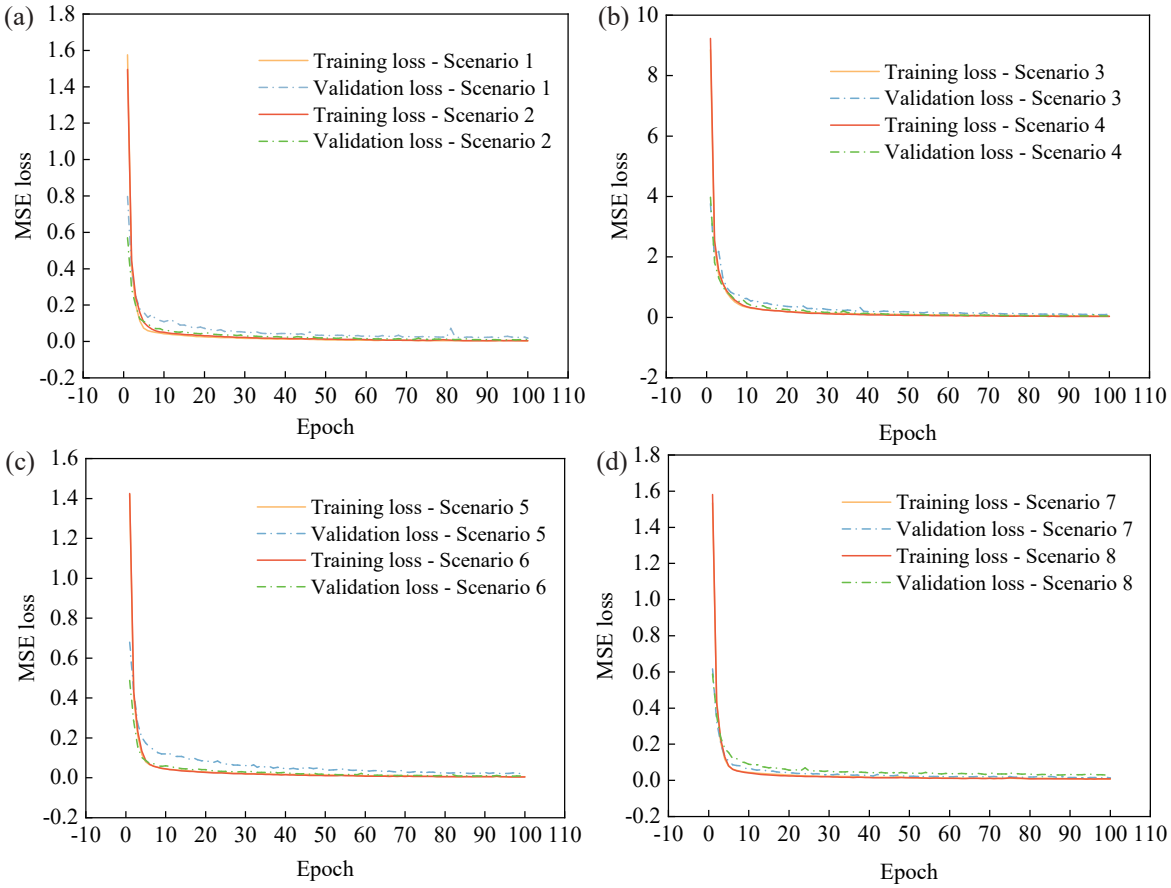

Fig. 6. The processes of training optimal models in Scenarios (a) 1 and 2, (b) 3 and 4, (c) 5 and 6, and (d) 7 and 8.

Table 7. Results of eight FCNNs within each scenario.

Model	MAE	MSE	MAPE
1	0.0213	0.0403	0.0576
2	0.0126	0.0437	0.0598
3	0.1168	0.1141	0.1268
4	0.1532	0.1687	0.1892
5	0.0130	0.0373	0.0476
6	0.0215	0.0523	0.0648
7	0.0279	0.0647	0.0792
8	0.0329	0.0488	0.0645

formance across all scenarios is detailed in Table 7.

First, the MSE, which measures the average squared difference between predicted and actual values, exhibits significant variability across the models, ranging from 0.0126 to 0.1532. This wide range highlights notable differences in predictive precision, with Model 2 achieving the lowest MSE, indicating peak accuracy, and Model 4 the highest, reflecting the poorest performance. Second, the MAE, assessing the average magnitude of prediction errors, ranges from 0.0373 to 0.1687. Unlike the MSE results, Model 5 records the lowest MAE, suggesting its predictions are, on average, closest to the actual values, while Model 4 again demonstrates the highest MAE, reinforcing its inferior performance. Third, the MAPE, representing average relative error, spans 0.0476 to 0.1892, with model 5 performs best by this metric, indicating superior proportional accuracy, particularly valuable where relative error matters. These findings suggest Scenario 4 poses the greatest challenge.

5.2.2 Generalization

The evaluation of the optimal models' generalizability included testing the performance of models trained on the Scenario A dataset against the test set from Scenario B, with full results in Table 8. The key findings are as follows:

1) Each model excels in its training scenario, confirming strong scenario-specific specialization.
2) No model consistently performs well across all scenarios; however, Models 3 and 4, trained on Scenarios 3 and 4, respectively, show moderate mutual generalization, suggesting shared features or conditions, a pattern also observed for Models 7 and 8.
3) Most models exhibit significantly poorer performance in untrained scenarios, notably Models 1 through 6 in Scenarios 3 and 4, and vice versa, indicating substantially differences between Scenarios 3 and 4 and the others. Overall, FCNN models display limited generalization ability in this task.

Table 8. Test results of FCNNs trained on scenarios 1 to 8.

Test set	Model 1	Model 2	Model 3	Model 4	Model 5	Model 6	Model 7	Model 8
1	0.0213	0.0146	2.4402	2.4428	0.0311	0.0248	0.0362	0.0510
2	0.0301	0.0126	2.4090	2.8834	0.0379	0.0353	0.0324	0.0325
3	2.5242	2.6476	0.1011	0.1532	4.6877	4.7203	4.8068	4.8092
4	2.5853	2.6605	0.1168	0.1012	4.6846	4.6919	4.7851	4.8562
5	0.0216	0.0243	2.4328	2.8096	0.0130	0.0325	0.0327	0.0363
6	0.0355	0.0303	2.4653	2.8551	0.0334	0.0131	0.0551	0.0364
7	0.0658	0.0493	2.4868	2.9222	0.0556	0.0541	0.0219	0.0253
8	0.0587	0.0497	2.4827	2.7664	0.0512	0.0539	0.0279	0.0106

6. Conclusion

This study introduces a method that integrating the LBM with FCNN to simulate complex water-rock dissolution reactions in submarine hydrothermal systems. The LBM-FCNN model features 31-dimensional input layer for physical quantities and an 11-dimensional output layer for dissolution state variables. An extensive hyperparameter search using the Optuna framework the optimized the network structure for this task. The model's generalizability was evaluated by testing its performance across diverse settings. It effectively simulates engineering environments with fracture apertures of 8 to 14 mm, adapting to varying roughness and reactive fluids. This approach combines LBM's physical accuracy with FCNN's computational efficiency, demonstrating the power of computational physics and machine learning.

For practical applications of this model, further training with data collected from real-world scenarios is required. Though, training with a combination of simulated and real-world data can effectively reduce the cost of data collection while ensuring relatively superior performance compared to using only real-world data. Future research will explore applying various neural network models to fields such as enhanced oil recovery, geothermal energy extraction, and environmental remediation.

Acknowledgements

This research is supported by the National Natural Science Foundation of China (No. 51936001) and the Demonstration and Guidance Project of Science and Technology Benefiting People in Qingdao, China (No. 22-3-7-cspz-6-nsh).

Conflict of interest

The authors declare no competing interest.

References

Akiba, T., Sano, S., Yanase, T., et al. Optuna: A next-generation hyperparameter optimization framework. Paper KDD 2623-2631 Presented at the Twenty fifth ACM SIGKDD International Conference on Knowledge Discovery & Data Mining, Anchorage, Alaska, 4-8 August, 2019.

Bhadauria, A., Dorschner, B., Karlin, I. Lattice Boltzmann method for fluid–structure interaction in compressible flow. Physics of Fluids, 2021, 33(10): 106111.

Chen, L., He, Y., Kang, Q., et al. Coupled numerical approach combining finite volume and lattice Boltzmann methods for multi-scale multi-physicochemical processes. Journal of Computational Physics, 2013, 255: 83-105.

Coronado, M., Ramírez-Sabag, J., Valdiviezo-Mijangos, O. Double-porosity model for tracer transport in reservoirs having open conductive geological faults: Determination of the fault orientation. Journal of Petroleum Science and Engineering, 2011, 78(1): 65-77.

El-Amin, M. F., Alwated, B., Hoteit, H. Machine learning prediction of nanoparticle transport with two-phase flow in porous media. Energies, 2023, 16(2): 678.

Elrahmani, A., Al-Raoush, R. I., Ayari, M. A. Modeling of permeability impairment dynamics in porous media: A machine learning approach. Powder Technology, 2024, 433: 119272.

Fu, S., Su, W., Zhang, H., et al. An immersed moving boundary for fast discrete particle simulation with complex geometry. Chemical Engineering Science, 2024, 283: 119407.

Gong, L., Han, D., Chen, Z., et al. Research status and development trend of key technologies for enhanced geothermal systems. Natural Gas Industry B, 2023, 10(2): 140-164.

He, H., Cao, J., Duan, N. Defects and their behaviors in mineral dissolution under water environment: A review. Science of the Total Environment, 2019, 651: 2208-2217.

Hinton, G. E., Osindero, S., Teh, Y. W. A fast learning algorithm for deep belief nets. Neural Computation, 2006, 18(7): 1527-1554.

Kamrava, S., Tahmasebi, P., Sahimi, M. Physics-and image-

based prediction of fluid flow and transport in complex porous membranes and materials by deep learning. Journal of Membrane Science, 2021, 622: 119050.

Kang, Q., Lichtner, P. C., Viswanathan, H. S., et al. Pore scale modeling of reactive transport involved in geologic CO_2 sequestration. Transport in Porous Media, 2010, 82(1): 197-213.

Liu, N., Liu, M. Simulation and analysis of wormhole propagation by VES acid in carbonate acidizing. Journal of Petroleum Science and Engineering, 2016, 138: 57-65.

Liu, X., Luo, X., Liu, S., et al. A numerical investigation of the nonlinear flow and heat transfer mechanism in rough fractured rock accounting for fluid phase transition effects. Water, 2024, 16(2): 342.

Lowell, R. P., Rona, P. A., Von Herzen, R. P. Seafloor hydrothermal systems. Journal of Geophysical Research: Solid Earth, 1995, 100(B1): 327-352.

Luo, Y., Feng, Y., Zhang, D., et al. Numerical simulation of chemical reactions' influence on convective heat transfer in hydrothermal circulation reaction zones. Energies, 2024, 17(11): 2442.

Mahmoodi, A., Javadi, A., Sola, B. S. Porous media acidizing simulation: New two-phase two-scale continuum modeling approach. Journal of Petroleum Science and Engineering, 2018, 166: 679-692.

Martín-Díaz, J. P., González-Vega, A., Barreyre, T., et al. Unveiling the inherent physical-chemical dynamics: Direct measurements of hydrothermal fluid flow, heat, and nutrient outflow at the Tagoro submarine volcano (Canary Islands, Spain). Science of the Total Environment, 2024, 918: 170565.

Micale, D., Ferroni, C., Uglietti, R., et al. Computational fluid dynamics of reacting flows at surfaces: Methodologies and applications. Chemie Ingenieur Technik, 2022, 94(5): 634-651.

Mohammadi-Arani, R., Dehghan, M., Abbaszadeh, M. Extending matrix–vector framework on multiple relaxation time lattice Boltzmann method. Applied Mathematics Letters, 2024, 152: 108998.

Salakhutdinov, R., Hinton, G. Deep Boltzmann machines. Paper PMLR 5: 448-455 Presented at the 12th International Conference on Artificial Intelligence and Statistics, Florida, America, 16-18 April, 2009.

Shan, X., Chen, H. Lattice Boltzmann model for simulating flows with multiple phases and components. Physical Review E, 1993, 47(3): 1815.

Sharma, K. V., Straka, R., Tavares, F. W. Current status of lattice Boltzmann methods applied to aerodynamic, aeroacoustic, and thermal flows. Progress in Aerospace Sciences, 2020, 115: 100616.

Spitzmüller, L., Goldberg, V., Held, S., et al. Selective silica removal in geothermal fluids: Implications for applications for geothermal power plant operation and mineral extraction. Geothermics, 2021, 95: 102141.

Wang, H., Chen, S. Insights into the application of machine learning in reservoir engineering: current developments and future trends. Energies, 2023, 16(3): 1392.

Wang, J., Guo, T., Chen, M., et al. Numerical simulation of deflagration fracturing in shale gas reservoirs considering the effect of stress wave impact and gas drive. International Journal of Rock Mechanics and Mining Sciences, 2023, 170: 105478.

Xie, Z., Huang, Z., Li, G., et al. The effect of natural fractures on the failure mechanism of granite: Implication for enhanced geothermal systems. Engineering Fracture Mechanics, 2024, 299: 109938.

Xi, L., Yin, D., Park, J. S. Special issue CFD modeling of complex chemical processes: Multiscale and multiphysics challenges. Processes, 2021, 9(5): 775.

Yamashita, R., Nishio, M., Do, R. K. G., et al. Convolutional neural networks: An overview and application in radiology. Insights into Imaging, 2018, 9: 611-629.

Yi, G., Zhuang, X., Li, Y. Probabilistic state estimation in district heating grids using deep neural network. Sustainable Energy, Grids and Networks, 2024, 38: 101353.

Zeng. H., Hu, P., He, Z., et al. Numerical simulation study of seafloor hydrothermal circulation based on hydrothermal foam: A case study of the wocan-1 hydrothermal field, Carlsberg ridge, Indian ocean. Journal of Marine Science and Engineering, 2023, 12(1): 46.

Zhang, D., Li, S., Jiao, S., et al. Relative permeability of three immiscible fluids in random porous media determined by the lattice Boltzmann method. International Journal of Heat and Mass Transfer, 2019, 134: 311-320.

Zhang, D., Li, S., Li, Y. Lattice Boltzmann simulation of three phase reactive flow in random porous media at pore-scale. Applied Thermal Engineering, 2021a, 194: 117140.

Zhang, D., Li, S., Li, Y. Pore-scale investigation on the effect of gas-liquid phase separation on reactive flow in a horizontal rough fracture using the lattice Boltzmann method. Chemical Engineering Science, 2021b, 236: 116483.

Zhou, J., Qi, B., Zhang, Y., et al. Experimental and theoretical study of bubble coalescence and departure behaviors during nucleate pool boiling on uniform smooth and micro-pin-finned surfaces under different sub-cooling and heat fluxes. Experimental Thermal and Fluid Science, 2020a, 112: 109996.

Zhou, X., Xu, Z., Xia, Y., et al. Pore-scale investigation on reactive flow in porous media with immiscible phase using lattice Boltzmann method. Journal of Petroleum Science and Engineering, 2020b, 191: 107224.